Journal of Power Sources 201 (2012) 288–293

Contents lists available at SciVerse ScienceDirect

Journal of Power Sources

journal homepage: www.elsevier.com/locate/jpowsour

Cooperative enhancement of capacities in nanostructured SnSb/carbon nanotube network nanocomposite as anode for lithium ion batteries

Shufen Fan [a], Ting Sun [a], Xianhong Rui [a,b], Qingyu Yan [a,c], Huey Hoon Hng [a,c,*]

[a] School of Materials Science and Engineering, Nanyang Technological University, Singapore 639798, Singapore
[b] School of Civil and Environmental Engineering, Nanyang Technological University, Singapore 639798, Singapore
[c] Energy Research Institute @ NTU, Nanyang Technological University, Singapore 638075, Singapore

ARTICLE INFO

Article history:
Received 18 August 2011
Received in revised form 8 October 2011
Accepted 26 October 2011
Available online 18 November 2011

Keywords:
Tin antimony
Carbon nanotubes
Nanocomposite
Melt spinning
Lithium ion batteries

ABSTRACT

SnSb-carbon nanotube nanocomposites are prepared by mixing melt-spun nanocrystalline SnSb with carbon nanotubes. The composite with 10 wt% acid functionalized CNTs shows a good initial Coulombic efficiency of 79% and a reversible capacity of 860 $mAhg^{-1}$ during the 40th cycle at a current density of 160 mAg^{-1}. Apart from that, the composite also shows promising capacities at high *C* rates. The enhancement is attributed to the synergistic effect between the nanocrystalline SnSb alloy and the CNT scaffold, which buffers the pulverization process and facilitates fast lithium ions diffusion.

1. Introduction

The ever increasing global energy demand coupled with the mandate to reduce carbon dioxide emission calls for more efficient and effective use of energy resources. The development of clean and renewable alternative energy sources as well as complementary energy storage and conversion systems are hence of utmost importance. Since its inception in the 1990s, lithium ion (Li-ion) batteries have been widely used as the power sources for portable electronic devices [1]. The ever-growing demands for LIBs, especially for high-energy and high-power applications such as electrical vehicles (EVs) and hybrid electrical vehicles (HEVs), have prompted numerous research efforts towards cost-effective and high-performance electrode materials [2,3]. Among the alternative anode materials, Li-alloy based elements such as silicon, tin, germanium, and antimony have attracted exceptional attentions due their ability to react reversibly with larger quantity of Li^+ per formula unit [4]. However, huge volume swing occurs (up to 400%) during the Li intercalation process of these materials, which leads to pulverization of the electrode and, consequently, rapid capacity fading.

Intermetallics of these alloys [5–9], such as $CoSb_3$, InSb, SnSb, and ZnSb, are also considered as promising candidates as the volume expansion is relatively smaller [2]. Furthermore, the Li intercalation voltages of these alloys are slightly higher than that of graphite, which favors operation safety. These intermetallic alloys can be classified into active/inactive and all active multiphase alloys. For inactive/active alloy, the alloy first decomposes irreversibly to the active metal that is dispersed in an inert matrix, and subsequently only the active metal takes part in the electrochemical reaction. The advantage is that the active component is produced in situ within the matrix and hence prevents the agglomeration of the active phase, albeit at the cost of reduced theoretical capacity and additional weight contributed by the inactive phase. On the other hand, all active multiphase alloys such as SnSb, offer several additional advantages. Firstly, since both Sn ($Li_{4.4}Sn$: 990 $mAhg^{-1}$) and Sb (Li_3Sb: 660 $mAhg^{-1}$) are active, they all contribute to the overall specific capacity. Secondly, due to the difference in reaction potential, the lithium insertion/extraction reactions will proceed in a stepwise manner. Work by Yang et al. [10] showed that lithium insertion will commence first with the more reactive phase (in this case, Sb) while the volume change of Sb can be accommodated for by the unreacted ductile Sn phase. In this way, severe volume change can be alleviated and mechanical stability of the electrode can be improved as compared to single phase Sn. During lithium insertion, the single-phase β-SnSb is transformed into Li_3Sb and multiple phases of Li_xSn ($x < 4.4$), which can be reversed back to the original β-SnSb upon lithium

* Corresponding author at: School of Materials Science and Engineering, Nanyang Technological University, Singapore 639798, Singapore. Tel.: +65 6790 4140; fax: +65 6790 9081.
E-mail address: ashhhng@ntu.edu.sg (H.H. Hng).

0378-7753/$ – see front matter © 2011 Elsevier B.V. All rights reserved.
doi:10.1016/j.jpowsour.2011.10.137

extraction [11]. Such a reversible structural variation is beneficial to the cyclic performance since one phase takes part in the reaction while the other acts as buffer against volume change. By nanostructuring this alloy, lithium ion and electron transport can be enhanced and large volume changes can also be partially relieved, giving rise to better cyclability and improved rate capability. However, nanostructured electrode may encounter the problem of agglomeration of nanocrystals due to the large surface energy, which leads to unstable cycling performance [12,13].

The formulation of composite electrode has been shown to be able to improve both capacity retention as well as rate capability, with carbon-based nanocomposite being the most widely investigated [14]. In such composites, the carbonanecous material is added as a conductive additive and plays the role of (i) preventing the agglomeration of the nanoparticles, (ii) providing structural support, and (iii) providing a percolated network to facilitate the transportation of ions and electrons. Among them, CNTs are promising due to its superior mechanical and electrical properties and hence, expected to better tolerate volume changes as compared to particle-to-particle contact network when carbon black is used [15,16]. Recent efforts to incorporate nanoscale Li-alloying materials such as Si, Sn and SnSb with CNTs have yield improvement in electrochemical performance. Processes such as CVD and various chemical synthesis methods were used to fabricate such composites [17–19]. However, such methods have low scalability and yield. Also, materials prepared by chemical synthesis may contain impurities, which led to fairly low initial Coulombic efficiency, due largely to the irreversibly consumption of lithium during the first discharge cycle. Melt spinning on the other hand, is a rapid solidification process with quench rate in the order of 10^6 K s^{-1}, and can result in materials with nanocrystalline or amorphous features with interesting material properties [20,21]. Furthermore, being a high throughput and scalable process, large quantity of high purity materials can be produced, which makes this process ready for industry level application. Hence, the advantage here is two-fold. Firstly, good initial Coulombic efficiency can be obtained. Secondly, the presence of nanocrystals and amorphous phases can contribute to the stability and fast rate capability.

In this study, we report the first effort on the preparation of nanocrystalline bulk SnSb via the melt spinning process. The as-spun nanostructured SnSb alloys were then mixed with CNTs to form SnSb-CNT composite material. The electrochemical characterization on these nanocomposites showed an improved initial Coulombic efficiency, high capacities and stable cyclability, e.g. 860 mAhg^{-1} during the 40th cycle at a current density of 160 mAg^{-1}.

2. Experimental procedures

2.1. Preparation of SnSb/CNT nanocomposite

Tin powder (99.9%, Goodfellow) and antimony powder (99.5%, Sigma–Aldrich) were weighed in the ratio of 1:1 and cold pressed into pellets. The nanostructured SnSb alloy is prepared from the pressed pellets using a single-roller melt-spinner (Edmund Bühler GmbH, Melt Spinner SC) with a 20 cm diameter copper wheel in an argon filled chamber. The distance between the bottom of the nozzle and the surface of the copper wheel was set at 0.5 mm, and the rolling rate of the wheel was 60 Hz. The precursor was induction melted to molten liquid and then pressure ejected through the slotted nozzle. Upon contact with the water-cooled wheel, the molten liquid rapidly solidified into very thin flakes.

The as-spun SnSb flakes were then triturated using the mortar grinder mill (Retsch, RM100) for 1 h to ensure a fine grinding. The obtained fine particles was then mixed with the acid treated CNTs (P3-SWNT, Carbon Solutions) in a weight ratio of 9:1 and dispersed in *N*-methylpyrrolidinone (NMP) and ultrasonicated for 1 h. It was then left to stir on a magnetic stirrer at 400 rpm for 2 days to ensure homogeneous mixing. The dispersion of the CNTs in solution is known to be a challenge as van der Waals interactions give rise to a strong tendency for the CNTs to agglomerate, bundle and entangle [22]. Several authors have shown the possibility of dispersing CNTs in amide based solutions, including NMP [23–25]. Hence, NMP was chosen as the dispersing agent for this work as it is also the solvent for the preparation of electrode material.

2.2. Characterization

Phase structures of the nanocomposites are investigated by powder X-ray diffraction (XRD) (Bruker AXS, D8 Advance) using Cu Kα radiation (λ = 0.15418 nm) over 2θ range of 10°–90°. Field emission scanning electron microscope (FESEM) (JEOL, JSM-7600F) and high-resolution transmission electron microscope (HRTEM) (JEOL, JEM-2100F) with energy dispersive X-ray spectroscopy (EDS) attachment are used for microstructure and elemental composition analysis of the melt spun flakes and nanocomposites before and after cycling. For microstructure analysis of the composite after cycling, the cell is dissembled in the glovebox, washed with dimethyl carbonate (DMC) to remove any residual electrolytes and left to dry prior to characterization. For HRTEM, the sample is first dispersed in ethanol and then dripped onto copper grid and dried at room temperature.

2.3. Electrochemical measurements

The anode are fabricated by mixing the SnSb-CNT composite, carbon black and poly(vinyldifluoride) (PVDF) dissolved in *N*-methylpyrrolidinone (NMP) at a weight ratio of 80:10:10. The slurry is then pasted onto the copper foil and dried in vacuum at 55 °C for 8 h. CR2032 coin-type batteries in the half-cell configuration were then assembled in an argon-filled glovebox with moisture and oxygen content less than 1 ppm. Lithium foil is used as the counter electrode and reference electrode, Celgard 2400 membrane as the separator and a solution of 1 M $LiPF_6$ in ethylene carbonate (EC)/dimethyl carbonate (DMC) (1/1, w w^{-1}) as the electrolyte. Cyclic voltammetry is performed with an electrochemical workstation (CHI 660C) at a scan rate of 0.5 mV s^{-1} in the potential range of 0.05–3.0 V. The cells were cycled galvanostatically between 0.05 and 3.00 V (vs. Li/Li^+) at various current densities using the NEWARE multi-channel battery test system.

3. Results and discussion

3.1. Phase and microstructures

The XRD pattern of the as-prepared sample through the melt spinning process is shown in Fig. 1. The results confirmed the formation of the rhombohedral β-SnSb phase (JCPDF 033-0018). The sharp peaks observed attested to the good crystallinity of the melt-spun flakes. No peaks corresponding to the impurity phase is observable in the XRD pattern. After triturating and mixing with CNTs, broadening of the (1 0 1) and (0 1 2) peaks of SnSb is observed, while no impurity phase is detected. The broadening of the peaks indicates that the grain size of the SnSb particles is reduced after triturating for 1 h. It is noted that the (0 0 2) and (1 0 0) reflections of the CNTs, which are located at 25.8° and 42.8° respectively [26], are obscured by the broadened (1 0 1) and (0 1 2) peaks of SnSb due to their close proximity. The grain size of the composite is estimated to be ~8 nm using the Scherrer formula from the (1 0 1) peak.

The SnSb sample from the melt spinning process is in the form of short flakes that are a few millimeters wide and a few centimeters

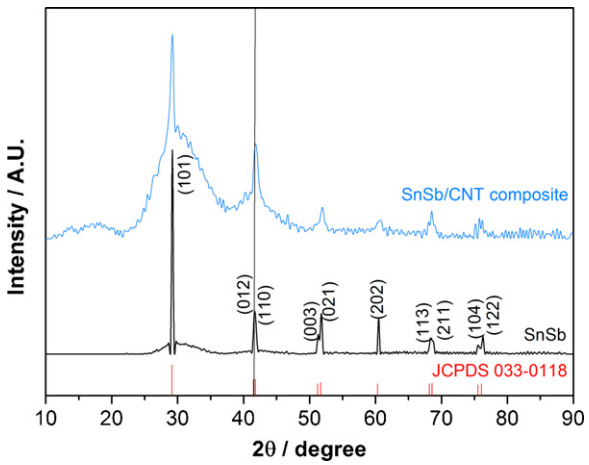

Fig. 1. XRD patterns of the melt spun SnSb alloy and SnSb-CNT composites.

long. Fig. 2 shows the SEM images of the representative morphology of the SnSb flakes. The free surface and contact surface (the face in contact with the copper wheel) showed different morphology as a result of the rapid quench rate and low thermal conductivity of the samples [27]. On the free surface, cubic-like structures that are a few micrometer as well as rod-like nanostructures that are less than 100 nm (Fig. 2a) are observed. On the other hand, due to the higher quench rate near the wheel's surface, the contact surface is almost featureless (Fig. 2b). HRTEM image (Fig. 2c) revealed that these as-spun flakes consisted of a mixture of nanograins that are a few nanometers. Fig. 2d shows the homogeneously mixed SnSb-CNT composite with the SnSb particles finely encrust within the mesh-like CNT framework, which consisted of well dispersed CNTs.

3.2. Electrochemical measurements

To study the Li-ion storage performance of the SnSb-CNT composites, a series of electrochemical measurements is carried out using the half cell configuration [28,29] in the potential range of 0.05–3.0 V (vs. Li/Li^+) at a current density of 160 mAg^{-1} (0.2*C*). Based on the theoretical capacity of SnSb, the current density of

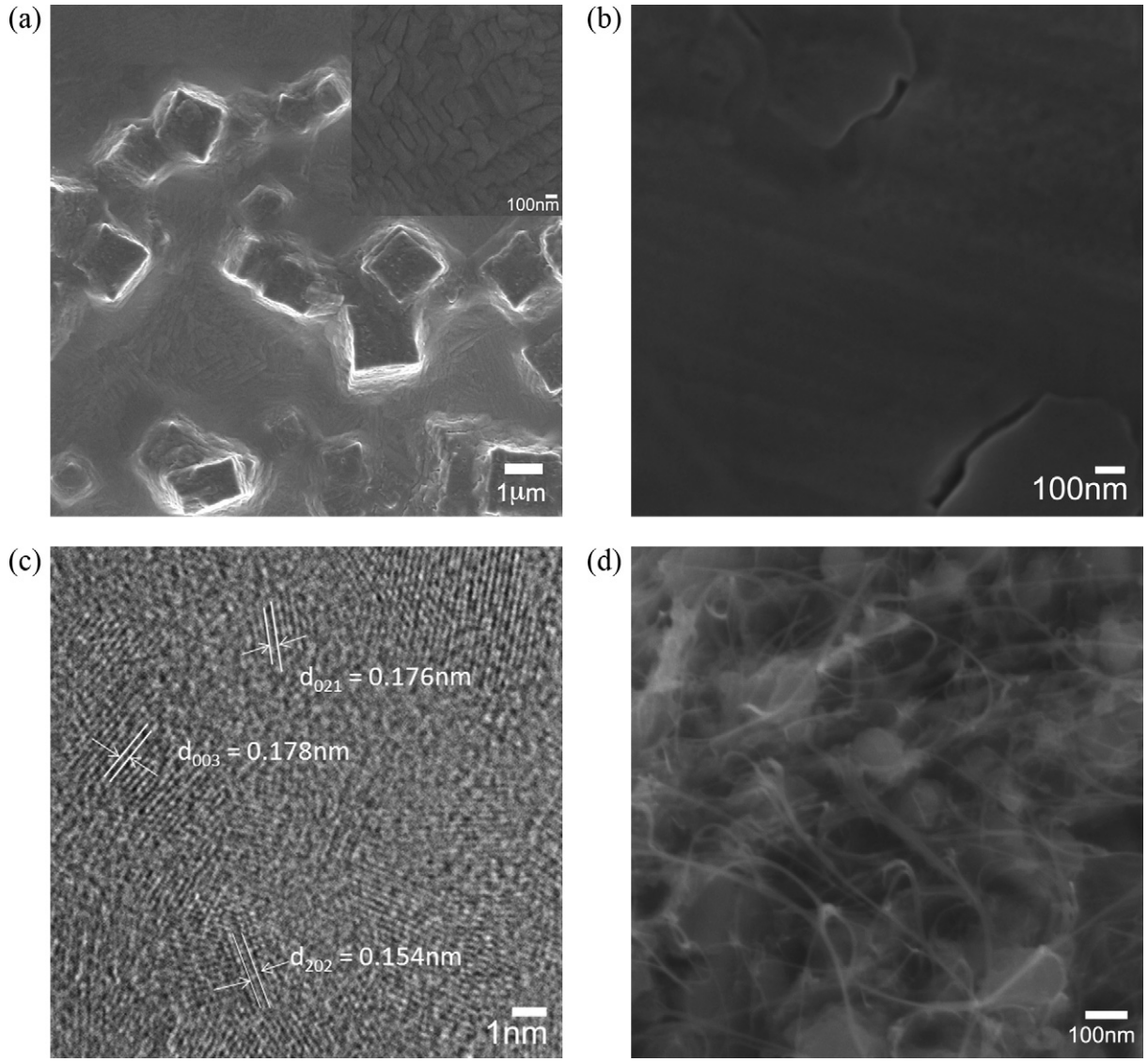

Fig. 2. Micrographs showing the (a) free surface with the insert showing the rod-like structures, (b) contact surface of the melt spun SnSb, (c) HRTEM image showing very fine SnSb grains and amorphous regions, and (d) the homogeneously mixed SnSb-CNT nanocomposite.

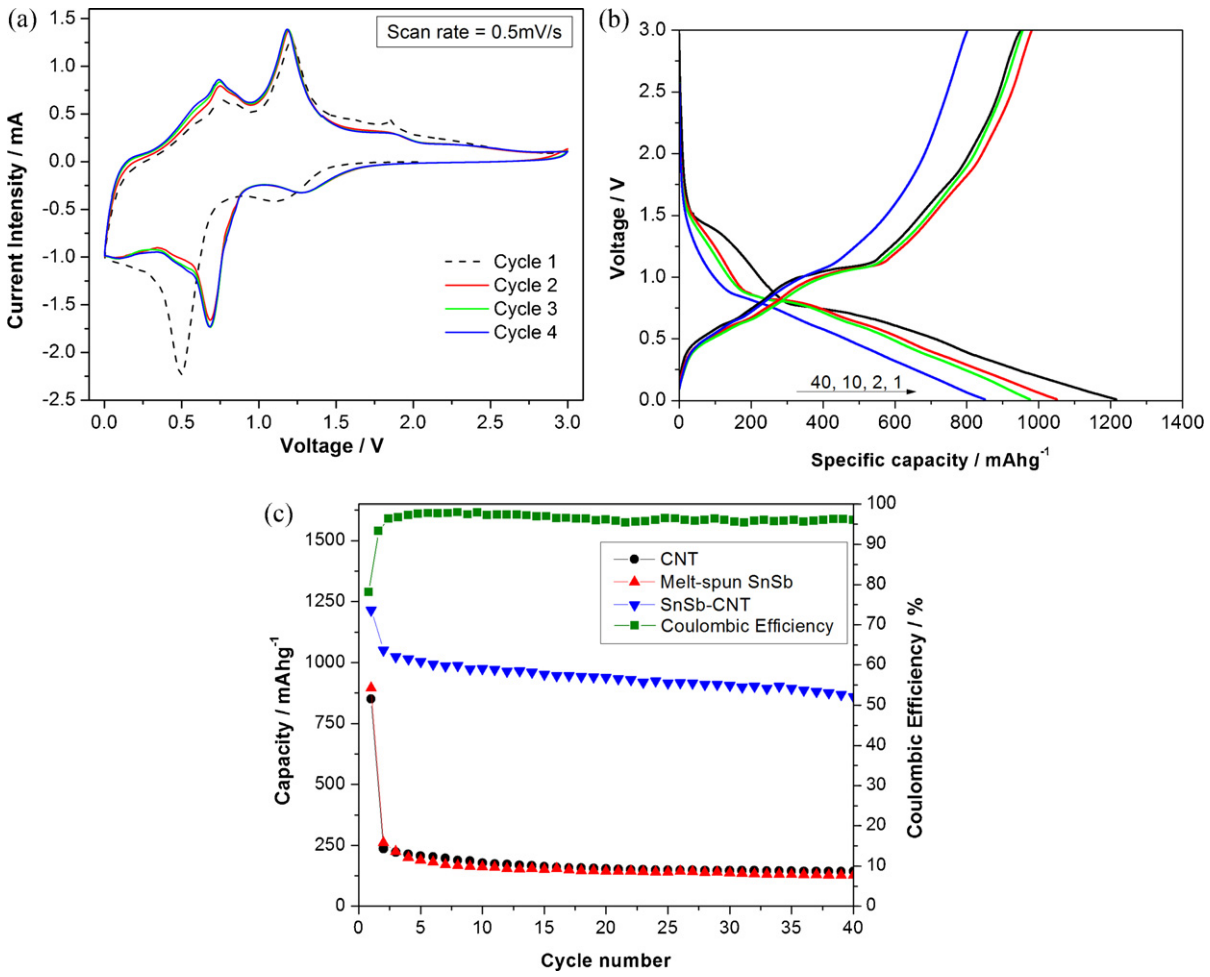

Fig. 3. (a) Cyclic voltammetry profile of the first 4 cycles of SnSb-CNT composite at a scan rate of 0.5 mV s^{-1}, (b) galvanostatic charge/discharge profiles at a current density of 160 mAg^{-1}, and (c) cycling performance of melt spun SnSb, CNTs and SnSb-CNT composite and its corresponding Coulombic efficiency.

824 mAg^{-1} is taken to be 1*C*. The cyclic voltammograms (CVs) profiles are shown in Fig. 3a. During the initial stage of lithiation process, a weak peak at around 1.13 V is observed, which is slightly higher than the characteristic voltage of lithium alloying with SnSb (0.8–0.9 V) [30]. It can be ascribed to the possible formation of a solid state solution of Li_xSnSb, where $0 < x < 1.6$, based on the calculated stable discharge capacity of 180 mAh^{-1} in the voltage range of 1.5–0.9 V (Fig. 3b). The existence of this ternary phase was demonstrated using ^{119}Sn and ^{121}Sb Mössbauer spectroscopy and X-ray diffraction [5,30]. The Li_xSnSb phase then reacts with more Li^+ ions to produce Li_3Sb in a highly ductile Sn matrix, which helps to relieve the mechanical strain associated with the expansion of the lattice during the formation of Li_3Sb [31], and followed by lithium alloying with Sn. In addition, the lithium insertion into CNTs can happen in the low voltage region around 0.2 V. These alloying and insertion processes are indicated by the strong reduction peak ranging from 0.8 to 0.1 V and the reactions are summarized as follows:

$$SnSb + xLi^+ + xe^- \leftrightarrow Li_xSnSb(0 < x < 1.6) \quad (1)$$

$$Li_{1.6}SnSb + 1.4Li^+ + 1.4e^- \leftrightarrow Li_3Sb + Sn \quad (2)$$

$$Sn + 4.4Li^+ + 4.4e^- \leftrightarrow Li_{4.4}Sn \quad (3)$$

$$yC + zLi^+ + ze^- \leftrightarrow Li_zC_y \quad (4)$$

During delithiation, the reaction sequence is reversed and SnSb is restored. The shoulders observed at 0.2 V are assigned to the extraction of lithium ions from the CNTs [32,33]. The de-alloying of Sn occurs between 0.4 and 0.8 V, followed by Sb at around 1.1 V. The ternary Li_xSnSb phase is then de-alloyed at around 1.85 V and SnSb is restored. The restoration of SnSb is beneficial in retarding the agglomeration of Sn into larger grains which has been identified as one of the key reasons for poor cycle stability of Sn-based materials [34].

The voltage profiles of the SnSb-CNT nanocomposite electrode in the potential range of 0.05–3.0 V at a current density of 160 mAg^{-1} (0.2*C*) are shown in Fig. 3b. The observed voltage plateaus are consistent with the CVs. An initial discharge capacity of 1215 mAh^{-1} and a subsequent charge capacity of 950 mAh^{-1} were obtained giving an initial Coulombic efficiency of 79%. This value is comparatively higher than those obtained in previous works on SnSb composite [32,35]. A high reversible discharge capacity of 860 mAh^{-1} is achieved during the 40th cycle, with a Coulombic efficiency of ~96%. In this work, the capacity obtained exceeded that of theoretical capacity. The extra capacity may be due to the long slope in the low voltage range (below 0.75 V), which contributes an extra Li storage capacity of ~550 mAh^{-1}. Similar phenomena were also observed in metal fluoride and transition metal oxide based anode materials [36,37]. The extra capacity contributed by the sloping region can be attributed to the reversible decomposition and the formation of a polymeric gel-like film over the surface of the active material as proposed by Tarascon et al. [37]. In addition, Li et al. [36] also proposed the possible interfacial interaction of lithium within the M/LiX matrix, which may also

lead to a distinct local charging, and gives rise to the extra Li storage capacity.

The cooperative effect between SnSb and CNTs can be seen more clearly from the cycling response curves in Fig. 3c. The SnSb-CNT composite exhibits a high initial Coulombic efficiency of 79% and a reversible capacity of 1050 $mAhg^{-1}$ with average Coulombic efficiency of 96%. As the composite electrode is a bi-percolating media which deals with ions and electrons transport, the microstructure as well as the selection of suitable conductive additive are vital to obtain composite with improved electrochemical performance [16]. The notable improvement of the initial Coulombic efficiency as well as the good cycability in this work can be attributed to two key factors: (1) the beneficial effects of conductive additive – CNT mesh-like network in ions and electrons transport [25,38,39], and (2) the high purity of the melt-spun SnSb alloy reduces the irreversible consumption of lithium and formation of SEI.

Subsequent cycling stability is contributed by the cooperative effective between the SnSb particles as well as the CNT mesh-like network. The SnSb particles are wrapped within the CNT mesh-like network, which greatly improves electrical conduction through the provision of a percolated pathway for electrons transport from the active material. Also, due to the presence of void spaces formed by the CNT network and the inherent mechanical flexibility of CNTs, the large volume variation can be buffered [25]. As the SnSb particles continue to be pulverized as cycling proceeds, the surface area increases. The increase in surface area improves the contact of the active material with the electrolyte, which shortens the ion diffusion path and hence, improves ionic transportation. The HRTEM image (Fig. 4a) showed the existence of SnSb particles of <5 nm in an amorphous matrix after repeated cycling and attest to the structural reversibility of SnSb, which contribute to the increase in Li^+ storage. Also, as observed, nanosized SnSb particles were pinned onto the surface of the CNTs (Fig. 4b), which further improve electron conduction and prevented the pulverized SnSb particles from aggregating, which might otherwise contribute to fast capacity fading. Hence, due to the structural adaptability of CNT to SnSb, the measured capacity of the composite is cooperatively enhanced, showing a good Coulombic efficiency of ~96% and higher than theoretical capacities in the cycles measured. Incidentally, capacity contribution from CNTs can be ignored, which exhibited a relatively low stable capacity of <150 $mAhg^{-1}$. In the contrary, the melt-spun SnSb showed large first cycle discharge capacity (900 $mAhg^{-1}$) that decreased drastically and stabilized below 150 $mAhg^{-1}$. This may be due to the poor adhesiveness of the electrode to the copper foil.

Gaberscek et al. [40] and Johns et al. [41] have demonstrated separately that high-rate performance not only relies on the minimization of the particle size of active materials, but also on the structure and composition of the composites, whereas Fongy et al. [42] demonstrated the effect of electrode porosity on rate performance. Rate capability of composite electrode is thus limited by the electronic and ionic wirings of the active mass and hence, the establishment of fast pathways to conduct ions and electrons from their reservoirs towards the active material are crucial for high-rate performance. Also, as proposed recently by Dalverny et al. [43] through first principles density function theory (DFT) calculations, interface migration is another reason for the improved kinetics of conversion and intermetallics compounds. The presence of very fine SnSb nanograins (<5 nm) resulted from the melt spinning process should be beneficial for fast lithium ion diffusion, while the highly interconnected CNT network should provide a good electronic percolation pathway, while at the same time provide some degree of electrode porosity for the diffusion of the electrolyte. This prompted us to also investigate on the rate capability of SnSb-CNT composite at various current densities (Fig. 5). Good Coulombic efficiency in the range of 96–98% were achieved over the cycles and current densities measured. The composite exhibited a high

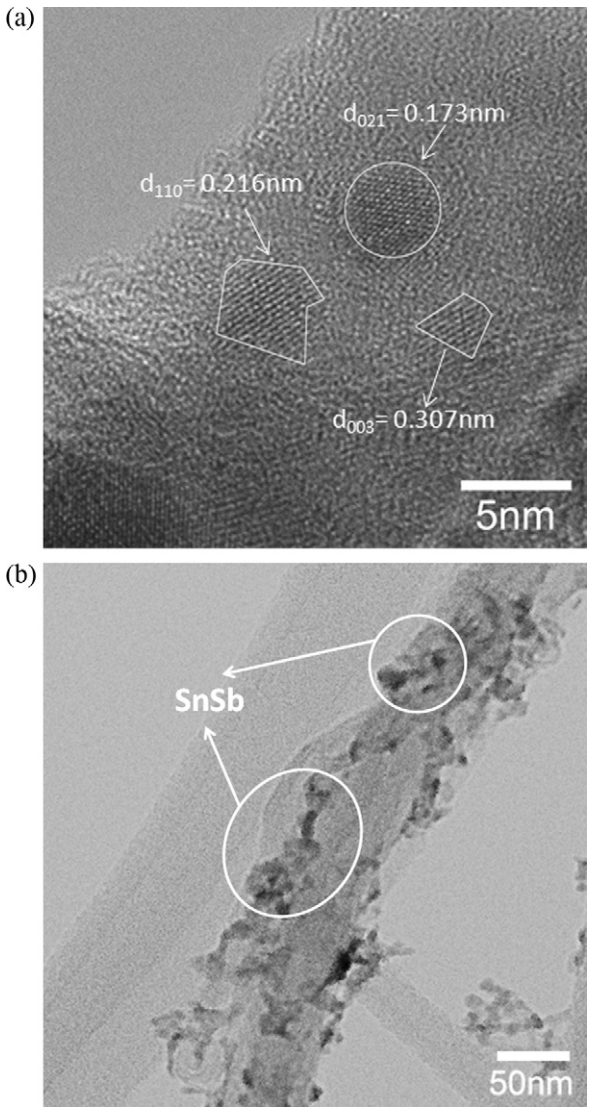

Fig. 4. (a) HRTEM image of SnSb-CNT showing the SnSb nanocrystals in an amorphous matrix, and (b) TEM image showing SnSb nanosized particles pinned onto CNT.

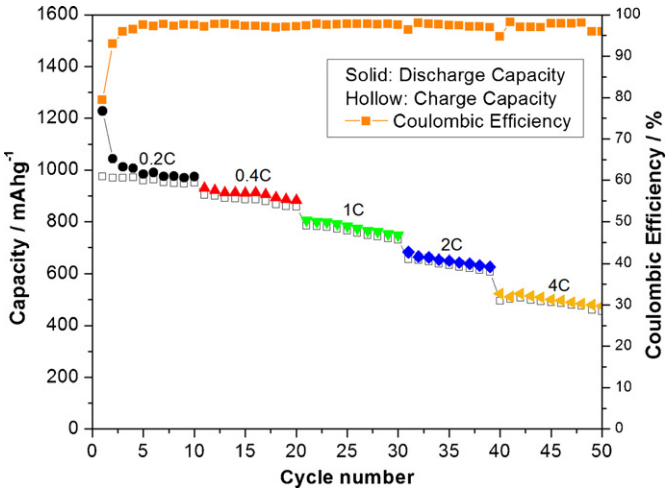

Fig. 5. Cycling performance of the SnSb-CNT composites at various current densities and its corresponding Coulombic efficiency.

capacity of 1050 mAhg^{-1} during the 2nd cycle at a current density of 160 mAg^{-1} (0.2*C*), which subsequently decreased to 930, 805 and 683 mAhg^{-1} at *C*-rate of 0.4*C*, 1*C* and 2*C* respectively. It is worth mentioning that even at a high current density of 4*C*, the SnSb-CNT composite is still able to deliver a high capacity of 522 mAhg^{-1}. Therefore, due to the presence of the mesh-like CNT network which ensures a good percolation conduction network, none of the electronic and ionic wirings of the active mass should limit the rate performance. Hence, the good rate performance demonstrated in this work comes from the inherent good rate capability of the active mass as a result of the melt spinning process. These values are higher than those reported previously for SnSb nanocomposites as well as the graphite anode (372 mAhg^{-1}) [32,35]. SnSb/CNT composite synthesized by reductive precipitation [32] shows a reversible capacity of 480 mAhg^{-1} at a current density of 100 mAg^{-1}, while the SnSb/C composite prepared by high energy mechanical milling shows a rate capability of 590 mAhg^{-1} and 550 mAhg^{-1} at 1*C* and 2*C* respectively [44]. The high rate capabilities demonstrated in this work, together with recent works on composites of other intermetallic compounds such as TiSnSb, $NiSb_2$, $FeSn_2$, shows that efficient percolation web formed by the conductive additive around the active particles is crucial in high-rate performance, and that intermetallic compounds do not have as much kinetics limitations as previously believed [45]. The high capacities obtained at high *C* rates indicate the possible applications of this SnSb-CNT composite for fast charge/discharge Li ion batteries.

4. Conclusion

In conclusion, we have demonstrated the feasibility of using a highly scalable and high throughput process of melt spinning to prepare the nanocrystalline bulk SnSb that were then mixed with CNT to form SnSb-CNT composite. The composites fabricated in this work demonstrated a good initial Coulombic efficiency of 79% and high reversible capacities, e.g. 860 mAhg^{-1} is achieved at the 40th cycle at 160 mAg^{-1}. Apart from that, the SnSb-CNT composite also showed good rate capability, e.g. high reversible capacity of 522 mAhg^{-1} is obtainable at a high current density of ~3300 mAg^{-1} (4*C*). The overall improvement in capacities is attributed to the cooperative effect between the nanocrystalline SnSb and CNTs. The CNT mesh-like network allows the diffusion of electrolyte into the matrix and at the same time provides percolated pathway for electrons and ions transport, while the nanocrystalline SnSb increases the surface area and contact with the electrolyte. Therefore, this work provides evidence that intermetallic compounds are not kinetics limited, and can be suited for high-rate applications.

Acknowledgement

The authors gratefully acknowledge the support of AcRF Tier 2 (MOE2010-T2-1-017) from MOE, Singapore.

References

[1] T. Nagaura, K. Tozawa, Progress in Batteries and Solar Cells 9 (1990) 209.
[2] J.M. Tarascon, M. Armand, Nature 414 (2001) 359–367.
[3] B. Scrosati, J. Hassoun, S. Yang-Kook, Energy and Environmental Science (2011) 3287–3295.
[4] C.-M. Park, J.-H. Kim, H. Kim, H.-J. Sohn, Chemical Society Reviews 39 (2010) 3115–3141.
[5] J.O. Besenhard, M. Wachtler, M. Winter, R. Andreaus, I. Rom, W. Sitte, Journal of Power Sources 81–82 (1999) 268–272.
[6] J. Yang, Y. Takeda, Q. Li, N. Imanishi, O. Yamamoto, Journal of Power Sources 90 (2000) 64–69.
[7] S. Saadat, Y.Y. Tay, J. Zhu, P.F. Teh, S. Maleksaeedi, M.M. Shahjamali, M. Shakerzadeh, M. Srinivasan, B.Y. Tay, H.H. Hng, J. Ma, Q. Yan, Chemistry of Materials 23 (2011) 1032–1038.
[8] J.X. Zhu, T. Sun, J.S. Chen, W.H. Shi, X.J. Zhang, X.W. Lou, S. Mhaisalkar, H.H. Hng, F. Boey, J. Ma, Q.Y. Yan, Chemistry of Materials 22 (2010) 5333–5339.
[9] S. Saadat, J. Zhu, M.M. Shahjamali, S. Maleksaeedi, Y.Y. Tay, B.Y. Tay, H.H. Hng, J. Ma, Q. Yan, Chemical Communications 47 (2011) 9849–9851.
[10] J. Yang, M. Winter, J.O. Besenhard, Solid State Ionics 90 (1996) 281–287.
[11] H. Li, G. Zhu, X. Huang, L. Chen, Journal of Materials Chemistry 10 (2000) 693–696.
[12] A.S. Arico, P. Bruce, B. Scrosati, J.-M. Tarascon, W. van Schalkwijk, Nature Materials 4 (2005) 366–377.
[13] P.G. Bruce, B. Scrosati, J.-M. Tarascon, Angewandte Chemie International Edition 47 (2008) 2930–2946.
[14] J. Yang, Y. Takeda, N. Imanishi, T. Ichikawa, O. Yamamoto, Solid State Ionics 135 (2000) 175–180.
[15] B.J. Landi, M.J. Ganter, C.D. Cress, R.A. DiLeo, R.P. Raffaelle, Energy and Environmental Science 2 (2009) 638–654.
[16] B. Lestriez, S. Desaever, J. Danet, P. Moreau, D. Plee, D. Guyomard, Electrochemical and Solid-State Letters 12 (2009) A76–A80.
[17] W. Wang, P.N. Kumta, ACS Nano 4 (2010) 2233–2241.
[18] Y. Wang, M. Wu, Z. Jiao, J.Y. Lee, Chemistry of Materials 21 (2009) 3210–3215.
[19] T. Prem Kumar, R. Ramesh, Y.Y. Lin, G.T.-K. Fey, Electrochemistry Communications 6 (2004) 520–525.
[20] A. Manaf, R.A. Buckley, H.A. Davies, M. Leonowicz, Journal of Magnetism and Magnetic Materials 101 (1991) 360–362.
[21] S. Fan, J. Zhao, J. Guo, Q. Yan, J. Ma, H.H. Hng, Applied Physics Letters 96 (2010) 182104.
[22] S.M. O'Flaherty, R. Murphy, S.V. Hold, M. Cadek, J.N. Coleman, W.J. Blau, The Journal of Physical Chemistry B 107 (2003) 958–964.
[23] T. Hasan, V. Scardaci, P. Tan, A.G. Rozhin, W.I. Milne, A.C. Ferrari, The Journal of Physical Chemistry C 111 (2007) 12594–12602.
[24] S.D. Bergin, V. Nicolosi, P.V. Streich, S. Giordani, Z. Sun, A.H. Windle, P. Ryan, N.P.P. Niraj, Z.-T.T. Wang, L. Carpenter, W.J. Blau, J.J. Boland, J.P. Hamilton, J.N. Coleman, Advanced Materials 20 (2008) 1876–1881.
[25] S. Park, T. Kim, S.M. Oh, Electrochemical and Solid-State Letters 10 (2007) A142–A145.
[26] C. Pirlot, I. Willems, A. Fonseca, J.B. Nagy, J. Delhalle, Advanced Engineering Materials 4 (2002) 109–114.
[27] W. Xie, J. He, H.J. Kang, X. Tang, S. Zhu, M. Laver, S. Wang, J.R.D. Copley, C.M. Brown, Q. Zhang, T.M. Tritt, Nano Letters 10 (2010) 3283–3289.
[28] J.X. Zhu, T. Zhu, X.Z. Zhou, Y.Y. Zhang, X.W. Lou, X.D. Chen, H. Zhang, H.H. Hng, Q.Y. Yan, Nanoscale 3 (2011) 1084–1089.
[29] J.X. Zhu, Y.K. Sharma, Z.Y. Zeng, X.J. Zhang, M. Srinivasan, S. Mhaisalkar, H. Zhang, H.H. Hng, Q.Y. Yan, Journal of Physical Chemistry C 115 (2011) 8400–8406.
[30] F.J. Fernández-Madrigal, P. Lavela, C.P. Vicente, J.L. Tirado, J.C. Jumas, J. Olivier-Fourcade, Chemistry of Materials 14 (2002) 2962–2968.
[31] I. Rom, M. Wachtler, I. Papst, M. Schmied, J.O. Besenhard, F. Hofer, M. Winter, Solid State Ionics 143 (2001) 329–336.
[32] M.-S. Park, S.A. Needham, G.-X. Wang, Y.-M. Kang, J.-S. Park, S.-X. Dou, H.-K. Liu, Chemistry of Materials 19 (2007) 2406–2410.
[33] S.-L. Chou, Y. Zhao, J.-Z. Wang, Z.-X. Chen, H.-K. Liu, S.-X. Dou, The Journal of Physical Chemistry C 114 (2010) 15862–15867.
[34] I.A. Courtney, J.R. Dahn, Journal of The Electrochemical Society 144 (1997) 2045–2052.
[35] S. Chen, P. Chen, M. Wu, D. Pan, Y. Wang, Electrochemistry Communications 12 (2010) 1302–1306.
[36] H. Li, G. Richter, J. Maier, Advanced Materials 15 (2003) 736–739.
[37] S. Laruelle, S. Grugeon, P. Poizot, M. Dolle, L. Dupont, J.-M. Tarascon, Journal of The Electrochemical Society 149 (2002) A627–A634.
[38] J. Shu, H. Li, R. Yang, Y. Shi, X. Huang, Electrochemistry Communications 8 (2006) 51–54.
[39] Y. Zhang, X.G. Zhang, H.L. Zhang, Z.G. Zhao, F. Li, C. Liu, H.M. Cheng, Electrochimica Acta 51 (2006) 4994–5000.
[40] M. Gaberscek, M. Kuzma, J. Jamnik, Physical Chemistry Chemical Physics 9 (2007) 1815–1820.
[41] P.A. Johns, M.R. Roberts, Y. Wakizaka, J.H. Sanders, J.R. Owen, Electrochemistry Communications 11 (2009) 2089–2092.
[42] C. Fongy, A.-C. Gaillot, S. Jouanneau, D. Guyomard, B. Lestriez, Journal of The Electrochemical Society 157 (2010) A885–A891.
[43] A.L. Dalverny, J.S. Filhol, M.L. Doublet, Journal of Materials Chemistry 21 (2011) 10134–10142.
[44] C.-M. Park, H.-J. Sohn, Electrochimica Acta 54 (2009) 6367–6373.
[45] V. Sivasankaran, C. Marino, M. Chamas, P. Soudan, D. Guyomard, J.C. Jumas, P.E. Lippens, L. Monconduit, B. Lestriez, Journal of Materials Chemistry 21 (2011) 5076–5082.